Land surface emissivity retrieval from different VNIR and TIR sensors

Article *in* IEEE Transactions on Geoscience and Remote Sensing · March 2008

DOI: 10.1109/TGRS.2007.904834 · Source: IEEE Xplore

8 authors, including:

Jose Sobrino
University of Valencia
306 PUBLICATIONS **8,107** CITATIONS
SEE PROFILE

Juan-Carlos Jimenez-Munoz
University of Valencia
132 PUBLICATIONS **3,371** CITATIONS
SEE PROFILE

Guillem Sòria Barres
University of Valencia
59 PUBLICATIONS **740** CITATIONS
SEE PROFILE

Luis Guanter
Helmholtz Centre Potsdam German Centre f…
157 PUBLICATIONS **3,492** CITATIONS
SEE PROFILE

Land Surface Emissivity Retrieval From Different VNIR and TIR Sensors

José A. Sobrino, Juan C. Jiménez-Muñoz, Guillem Sòria, Mireia Romaguera, Luis Guanter, José Moreno, *Associate Member, IEEE*, Antonio Plaza, *Senior Member, IEEE*, and Pablo Martínez

***Abstract*—This paper discusses the application and adaptation of two existing operational algorithms for land surface emissivity (ε) retrieval from different operational satellite/airborne sensors with bands in the visible and near-infrared (VNIR) and thermal IR (TIR) regions: 1) the temperature and emissivity separation algorithm, which retrieves ε only from TIR data and 2) the normalized-difference vegetation index thresholds method, in which ε is retrieved from VNIR data.**

***Index Terms*—Fractional vegetation cover (FVC), land surface emissivity, normalized difference vegetation index (NDVI), temperature and emissivity separation (TES), thermal infrared (TIR).**

I. Introduction

LAND SURFACE emissivity (ε) is a proportionality factor that scales blackbody radiance (Planck's law) to predict emitted radiance, and it is the efficiency of transmitting thermal energy across the surface into the atmosphere. In this sense, ε must be known in order to estimate land-surface temperature accurately from radiance measurements. Knowledge of the ε spectrum is also useful for terrestrial and planetary geologic studies to map surface materials based on differences in wavelength-dependent spectral features [1].

The recovery of ε from thermal infrared (TIR) remotely sensed data requires the solution of two main problems: 1) the radiances measured by the sensor are affected by the contribution of the atmosphere (absorption and reemission by atmospheric gases, mainly water vapor in the TIR region) and 2) the underdetermined nature of thermal measurements, in which temperature and emissivity are coupled (for N spectral bands, there will be $N+1$ unknowns, N emissivities, plus a single land-surface temperature). The first problem refers to the atmospheric correction or compensation, whereas the second problem refers to the temperature and emissivity separation (TES). From a theoretical point of view, these problems can be dealt with the radiative-transfer equation applied to a certain wavelength (λ) in the TIR region

$$L_\lambda = \varepsilon_\lambda B_\lambda(T_s)\tau_\lambda + (1-\varepsilon_\lambda)L_{d\lambda}\tau_\lambda + L_{u\lambda} \tag{1}$$

where L is the radiance reaching the sensor from the ground surface, $B(T_\mathrm{s})$ is the Planck radiation function, τ is the atmospheric transmittance for the path between the surface and the sensor, L_u is the upwelling atmospheric radiance for the same path, and L_d is the hemispherical downwelling radiance from the entire sky. All these spectral variables represent average values according to the filter functions of the sensor bands considered. The first term on the right side in (1) is the surface emission attenuated by the atmosphere, the second term is the ground-reflected atmospheric radiance also attenuated by the atmosphere, and the third term is the atmospheric emission itself. If we consider the radiance coming from the surface (effective surface radiance or land-leaving radiance) as

$$L_{s\lambda} = \varepsilon_\lambda B_\lambda(T_s) + (1-\varepsilon_\lambda)L_{d\lambda} \tag{2}$$

(2) becomes

$$L_\lambda = L_{s\lambda}\tau_\lambda + L_{u\lambda} \tag{3}$$

and, then, the atmospheric compensation reduces to

$$L_{s\lambda} = \frac{L_\lambda - L_{u\lambda}}{\tau_\lambda}. \tag{4}$$

The quantity L_s, which is given by (2), shows, explicitly, the coupling between ε and T_s, but it also shows that there still remains an atmospheric contribution, which is coupled to the emissivity. This fact can be considered as a third problem in the recovery of ε from TIR data.

Even when the atmospheric parameters (τ, L_d, and L_u) are known, because of the coupling between ε and T, a number of methods have been explored to constrain the extra degree of freedom, among others, the Alpha-Derived Emissivity (ADE) method [2], Day/Night Methods (DNM) [3], Emissivity Bounds Method (EBM) [4], Graybody Emissivity Method (GEM) [5], mean Maximum–Minimum-Difference (MMD) method [6], Reference-Channel Method (RCM) [7], Normalized-Emissivity Method (NEM) [8], Ratio Algorithm (RA) [9], Temperature-Independent Spectral Indices (TISI)

Manuscript received February 14, 2007; revised June 22, 2007. This work was supported in part by European Union (EAGLE, Project SST3-CT-2003-502057), by the Ministerio de Ciéncia y Tecnología (DATASAT, Project ESP2005-07724-C05-04), and by the Generalitat Valenciana (Conselleria d'Empresa, Universitat i Ciència, Project ACOMP06/219).

J. A. Sobrino, J. C. Jiménez-Muñoz, G. Sòria, and M. Romaguera are with the Global Change Unit, Department of Earth Physics and Thermodynamics, University of Valencia, 46100 Burjassot, Spain (e-mail: sobrino@uv.es).

L. Guanter and J. Moreno are with the Laboratory of Earth Observation, Department of Earth Physics and Thermodynamics, University of Valencia, 46100 Burjassot, Spain.

A. Plaza and P. Martínez are with the Neural Network and Signal Processing Group, Computer Science Department, University of Extremadura, 10071 Cáceres, Spain.

Color versions of one or more of the figures in this paper are available online at http://ieeexplore.ieee.org.

Digital Object Identifier 10.1109/TGRS.2007.904834

[10], or methods based on Image CLassification (ICL) [11]. Most of the constraints of these methods were analyzed in the study in [12]. Briefly, DNM require acquisitions twice a day and perfectly coregistered, and they assume that day/night emissivity differences are negligible, which is not usually true due to dew (except for arid regions); ADE, RCM, NEM, RA, and TISI methods only provide relative emissivity values; ICL methods require *a priori* knowledge of the emissivity values to be assigned to each class; EBM also needs *a priori* knowledge of emissivity; the assumption involved in the GEM of graybody behavior is not usually accomplished; the MMD method is useful for retrieving emissivities, but it is included and improved in the TES algorithm that will be presented later.

The limitations of the different existing methods and the availability of multispectral TIR data foreseen with the launch of the Advanced Spaceborne Thermal Emission and Reflection Radiometer (ASTER) led to the development of a new algorithm in determining land-surface temperatures and the emissivity spectra, which is referred to as TES algorithm [12]. Since the TES algorithm requires multispectral TIR data, methods based on normalized difference vegetation index (NDVI) estimations from visible and near-infrared (VNIR) data have been also developed for applications to sensors without multispectral TIR capabilities, as for example, the NDVI THresholds Method ($\mathrm{NDVI}^{\mathrm{THM}}$) [13]. TES and $\mathrm{NDVI}^{\mathrm{THM}}$ are very useful for retrieving surface emissivities from remote-sensing data collected by sensors onboard satellites in an operational way, and the authors think that these two methods are currently the best candidates for this purpose, despite that TES and $\mathrm{NDVI}^{\mathrm{THM}}$ algorithms fail for graybodies and senescent vegetation, respectively.

This paper presents an overview of the application of TES algorithm and $\mathrm{NDVI}^{\mathrm{THM}}$ in recovering surface emissivities from different operational sensors, as well as its application to airborne sensors used in different field campaigns. Methods for retrieving ε from ground-based measurements are also reminded, which can be useful to obtain "ground-truth" data to test the results extracted from remote-sensing images.

II. Description of Methods

A. TES Algorithm

TES algorithm was developed by the authors of [12] to produce Standard Products of surface temperature and emissivity from ASTER data. It uses land-leaving radiance (2) and downwelling sky irradiance (L_{d}) as input, providing a first guess for surface temperatures and emissivities using the NEM. The results are improved by applying another two modules: the RATIO module, which computes relative emissivities (beta spectrum), and the MMD module, which uses a semiempirical relation determined from laboratory spectra, between the minimum emissivity and spectral contrast (MMD). Despite the fact that the TES method was designed to retrieve surface emissivities within about 0.015 and surface temperatures within about 1.5 K, some problems have been found due to inaccuracies in atmospheric compensation, and inaccuracies over some surfaces was not accomplished using the relation between minimum emissivity and MMD [14], [15]. Some modifications to the algorithm have been tested to solve, in part, these problems [16]. The TES algorithm requires multispectral TIR data (at least four TIR bands) to work.

B. NDVI Thresholds Method

Different approaches have been used to predict land surface emissivity from NDVI values [17], [18]. In this section, we describe the $\mathrm{NDVI}^{\mathrm{THM}}$, which is first introduced by [13] and applied to Advanced Very High Resolution Radiometer (AVHRR) data, and later compared with other methods and adapted to other sensors, as will be commented later.

$\mathrm{NDVI}^{\mathrm{THM}}$ uses certain NDVI values (thresholds) to distinguish between soil pixels ($\mathrm{NDVI} < \mathrm{NDVI_s}$) and pixels of full vegetation ($\mathrm{NDVI} > \mathrm{NDVI_v}$). For those pixels composed of soil and vegetation (mixed pixels, $\mathrm{NDVI_s} \leq \mathrm{NDVI} \leq \mathrm{NDVI_v}$), the method uses the following simplified equation:

$$\varepsilon_\lambda = \varepsilon_{\mathrm{v}\lambda} P_V + \varepsilon_{s\lambda}(1 - P_V) + C_\lambda \tag{5}$$

where ε_{v} and ε_{s} are, respectively, the soil and vegetation emissivities, P_{V} is the proportion of vegetation (also referred to as fractional vegetation cover, FVC), and C is a term which takes into account the cavity effect due to surface roughness ($C = 0$ for flat surfaces). Using the geometrical model proposed by the authors in [19], the cavity term for a mixed area and near-nadir view is given by

$$C_\lambda = (1 - \varepsilon_{s\lambda})\varepsilon_{\mathrm{v}\lambda} F'(1 - P_V) \tag{6}$$

where F' is a geometrical factor ranging between zero and one, depending on the geometrical distribution of the surface. Since F' cannot be estimated from VNIR/TIR remote-sensing data, a mean value is generally chosen [13].

P_{V} values are obtained from the NDVI according to [20]

$$P_V = \left(\frac{\mathrm{NDVI} - \mathrm{NDVI}_s}{\mathrm{NDVI}_V - \mathrm{NDVI}_s} \right)^2. \tag{7}$$

Over particular areas, $\mathrm{NDVI_v}$ and $\mathrm{NDVI_s}$ values can be extracted from the NDVI histogram. Values of $\mathrm{NDVI_v} = 0.5$ and $\mathrm{NDVI_s} = 0.2$ were proposed by the authors in [13] to apply the method in global conditions. In order to obtain consistent values of P_{V}, it must be set to zero for pixels with $\mathrm{NDVI} < \mathrm{NDVI_s}$ and set to one for pixels with $\mathrm{NDVI} > \mathrm{NDVI_v}$.

When $\mathrm{NDVI} > \mathrm{NDVI_v}$, the pixel is considered as fully vegetated ($P_{\mathrm{V}} = 1$), and then, (5) reduces to $\varepsilon_\lambda = \varepsilon_{\mathrm{v}\lambda} + C_\lambda$. Typical constant values of $\varepsilon_{\mathrm{v}} = 0.985$ and $C = 0.005$ are considered for these kind of pixels, so a value of 0.99 for fully vegetated pixels is finally set. Note that (6) is only valid for a mixed area, so this expression does not reflect the cavity effects produced in a rough but homogeneous area.

$\mathrm{NDVI}^{\mathrm{THM}}$ estimates the surface emissivity for pixels of bare soil ($\mathrm{NDVI} < \mathrm{NDVI_s}$) from reflectivity values (ρ_{red}) obtained with a sensor band located in the red region (for example, using AVHRR band 1). The relationship between emissivities and red reflectivities is assumed to be linear, and the coefficients are

obtained from laboratory spectra of soils and statistical fits. The $\mathrm{NDVI}^{\mathrm{THM}}$ can be summarized as follows:

$$\varepsilon_\lambda = \begin{cases} a_\lambda + b_\lambda \rho_{\mathrm{red}}, & \mathrm{NDVI} < \mathrm{NDVI}_s \\ \varepsilon_{\mathrm{v}\lambda} P_V + \varepsilon_{s\lambda} \\ \quad \times (1 - P_V) + C_\lambda, & \mathrm{NDVI}_s \leq \mathrm{NDVI} \leq \mathrm{NDVI}_{\mathrm{v}} \\ \varepsilon_{\mathrm{v}\lambda} + C_\lambda, & \mathrm{NDVI} > \mathrm{NDVI}_{\mathrm{v}}. \end{cases} \tag{8}$$

The problem of the $\mathrm{NDVI}^{\mathrm{THM}}$ described until now is the lack of continuity for emissivity values at $\mathrm{NDVI} = \mathrm{NDVI}_{\mathrm{s}}$, since they are calculated in different ways. The continuity at $\mathrm{NDVI} = \mathrm{NDVI}_{\mathrm{v}}$ is not guaranteed neither, since the cavity term given by (6) is not applicable when $\mathrm{NDVI} > \mathrm{NDVI}_{\mathrm{v}}$, as has been highlighted before. In addition, the estimation of the cavity term from remote-sensing data is a critical question, and the method only provides acceptable results in the 10–12-μm interval. Thus, the relation between ε and ρ_{red} for bare-soil samples does not provide satisfactory results for band emissivities at 8–9.5 μm in certain kind of soils. These problems can be formally solved by simplifying the $\mathrm{NDVI}^{\mathrm{THM}}$ presented in (8). For this purpose, the cavity term is not considered, and the expression for the surface emissivity when $\mathrm{NDVI} < \mathrm{NDVI}_{\mathrm{s}}$ is just reduced to the soil emissivity. These simplifications, hereinafter referred to as $\mathrm{SNDVI}^{\mathrm{THM}}$ (simplified $\mathrm{NDVI}^{\mathrm{THM}}$), are summarized as follows:

$$\varepsilon_\lambda = \begin{cases} \varepsilon_{s\lambda}, & \mathrm{NDVI} < \mathrm{NDVI}_s \\ \varepsilon_{s\lambda} + (\varepsilon_{\mathrm{v}\lambda} - \varepsilon_{s\lambda}) P_V, & \mathrm{NDVI}_s \leq \mathrm{NDVI} \leq \mathrm{NDVI}_{\mathrm{v}} \\ \varepsilon_{\mathrm{v}\lambda}, & \mathrm{NDVI} > \mathrm{NDVI}_{\mathrm{v}}. \end{cases} \tag{9}$$

It can be observed that continuity at $\mathrm{NDVI} = \mathrm{NDVI}_{\mathrm{s}}$ ($P_{\mathrm{V}} = 0$) and $\mathrm{NDVI} = \mathrm{NDVI}_{\mathrm{v}}$ ($P_{\mathrm{V}} = 1$) is accomplished in (9), but the application of the $\mathrm{SNDVI}^{\mathrm{THM}}$ requires the knowledge of the soil-emissivity spectrum when $\mathrm{NDVI} < \mathrm{NDVI}_{\mathrm{s}}$. In theory, over mixed pixels ($\mathrm{NDVI}_{\mathrm{s}} \leq \mathrm{NDVI} \leq \mathrm{NDVI}_{\mathrm{v}}$), the $\mathrm{NDVI}^{\mathrm{THM}}$ could use soil emissivities estimated from red reflectivity over neighboring pixels accomplishing $\mathrm{NDVI} < \mathrm{NDVI}_{\mathrm{s}}$ as input, thus, without requiring *a priori* knowledge of soil emissivities. However, in practice, mean values are chosen in order to apply (8) to mixed pixels. In this case, the soil influence is lower with increasing P_{V}, and for low-resolution sensors with bands located in the 10–12-μm spectral region, variations of soil emissivity are low, which justifies the selection of a mean value.

Note that $\mathrm{NDVI}^{\mathrm{THM}}$ (or $\mathrm{SNDVI}^{\mathrm{THM}}$) can be applied over surfaces composed by soil and vegetation. Over surfaces like water, ice, or snow, one can apply another NDVI threshold (e.g., $\mathrm{NDVI} < 0$ for water) or use other indexes to discriminate these kind of pixels and, then, to assign emissivity values, which are commonly well known for these areas. Problems arise over other kind of surfaces, such as rocks, which could be classified as bare-soil pixels (except for rocks with a spectrum falling within the linear relation with ρ_{red} in the case of the $\mathrm{NDVI}^{\mathrm{THM}}$ or rocks with a similar spectrum than the chosen soil in the case of the $\mathrm{SNDVI}^{\mathrm{THM}}$). This problem is somehow minimized when working with low spatial resolution data, since it is not common to find rocks at 1-km scale.

C. Methods for Emissivity Retrieval From Ground-Based Measurements

It is important to retrieve surface emissivities from ground-based measurements, since they could be used to test the emissivity products obtained from remote-sensing data after applying one of the existing algorithms. *In situ* measurements of bare soils can be also used as input in the $\mathrm{NDVI}^{\mathrm{THM}}$ or $\mathrm{SNDVI}^{\mathrm{THM}}$. Emissivity spectra of terrestrial materials can be measured using sophisticated procedures, as, for example, the directional hemispherical reflectance measurements carried out with a spectrometer in the laboratory and converted to emissivities using the Kirchhoff's law [21], [22]. However, in this section, we will refer to methods that allow the emissivity retrieval from field (or laboratory) measurements carried out with commercial radiometers and accessible mechanisms of low or moderate cost. For this purpose, the box method [23] and the TES algorithm applied to ground-based measurements [24], [25] has been considered. The box method can be also used in the laboratory *per se*, whereas the TES algorithm can be applied in the laboratory after heating the sample to minimize the effect of the environmental irradiance. The TES algorithm can be also applied to laboratory measurements without heating the sample using measurements carried out with the box as input [25]. Note that the box method can be applied to any thermal band, whereas the TES algorithm requires four or five TIR narrow bands.

III. Imagery and Field Data

A. Satellite Sensors

The methods discussed in this paper have been applied to the following well-known operational sensors: AVHRR onboard the National Oceanic Atmospheric Administration platform; Advanced Along Track Scanning Radiometer (AATSR) onboard the ENVIronmental SATellite; Spinning Enhanced Visible and IR Imager (SEVIRI) onboard the Meteosat Second Generation (MSG1/Meteosat-8); Moderate Resolution Imaging Spectrometer (MODIS) onboard the TERRA and AQUA platforms; Thematic Mapper (TM) onboard the LANDSAT-5 platform; Compact High-Resolution Imaging Spectrometer (CHRIS) onboard the PRoject for OnBoard Autonomy (PROBA) platform; and the ASTER onboard the TERRA platform.

AVHRR and AATSR are low-resolution sensors, with a spatial resolution of around 1 km and two TIR bands. Both sensors have at least two VNIR bands, which is useful for computing the NDVI (bands 1 and 2 in the case of AVHRR and bands 2 and 3 in the case of AATSR). SEVIRI sensor is also a low-resolution sensor (pixel size of 3 km at nadir) with five TIR bands in the 8–14-μm spectral region. However, two TIR bands are located in the absorption regions (ozone at 9.7 μm and carbon dioxide at 13.4 μm). NDVI can be calculated from bands 1 and 2, or VIS0.6 and VIS0.8, following notation provided by the Organization for the Exploitation of Meteorological Satellites. MODIS sensor has 36 spectral bands, with a spatial resolution for bands 1 and 2 (the ones used for NDVI calculations) of 250 m. It has eight TIR bands

TABLE I
NUMBER OF VNIR AND TIR BANDS AND SPATIAL RESOLUTION FOR THE SATELLITE SENSORS CONSIDERED IN THIS PAPER. CHRIS CHARACTERISTICS REFER TO ACQUISTION MODE 1

PLATFORM/ SENSOR	VNIR bands (0-1.5 μm)	TIR bands (8-14 μm)	Spatial Resolution (m)
LANDSAT5/TM	4	1	60 (VNIR) 120 (TIR)
NOAA/AVHRR	2	2	1000
ENVISAT/AATSR	2	2	1000
MSG1/SEVIRI	2	5	3000
TERRA/MODIS AQUA/MODIS	17	8	250-500 (VNIR) 1000 (TIR)
PROBA/CHRIS	62	0	34
TERRA/ASTER	3	5	15 (VNIR) 90 (TIR)

(from 29 to 36) in the 8–14-μm spectral region, with a spatial resolution of 1 km, but only bands 29, 31, and 32 are located in an atmospheric window.

LANDSAT-5 TM is a multispectral and high/moderate-spatial-resolution sensor with six bands located in the VNIR/ Short Wave IR (SWIR) region (bands 3 and 4 being the ones used in the NDVI), with a spatial resolution of 30 m, and one TIR band (band 6) with a spatial resolution of 120 m. LANDSAT-7 Enhanced TM Plus data improves the spatial resolution of TM thermal band, with 60 m, and it also includes a panchromatic band (15 m). Technical problems associated with this sensor have limited its use in quantitative analysis, so it is not included in this paper.

PROBA–CHRIS system is a technology-demonstration experiment to take advantage of autonomous pointing capabilities of a generic platform for Earth-observation purposes. It provides high spatial resolution hyperspectral/multiangular data. CHRIS measures over the VNIR bands from 400 to 1050 nm, with a minimum spectral sampling interval ranging between 1.25 (at 400 nm) and 11 nm (at 1000 nm). It can operate in different modes, thus compromising the number of spectral bands and the spatial resolution because of storage reasons. CHRIS images, used in this paper, were acquired in Mode 1 (62 spectral bands and 34 m as spatial resolution).

ASTER is the only satellite sensor with multispectral TIR capabilities needed for applying the TES algorithm. It has three VNIR bands (two and three used in the NDVI) with a spatial resolution of 15 m, nine SWIR bands at 30 m, and five TIR bands at 90 m.

Table I provides a brief summary of the number of VNIR and TIR bands for these sensors, as well as the spatial resolution.

B. Airborne Sensors

Airborne imagery collected in the framework of different field campaigns and over particular areas has also been used in this paper. Airborne sensors have a better spectral resolution than satellite sensors, and due to low altitude in which the flights are performed, they provide high spatial resolution images, with pixel sizes of only a few meters. In this case, we have used the Digital Airborne Imaging Spectrometer (DAIS) and the Airborne Hyperspectral Scanner (AHS).

DAIS sensor is a high-resolution optical spectrometer operated by the German Aerospace Center. It has 79 bands covering

TABLE II
DAIS SPECTRAL CHARACTERISTICS. VALUES OF EFFECTIVE WAVELENGTH FOR TIR BANDS ARE ALSO GIVEN

Wavelength Range (μm)	Bands	Number of bands	Band-Width (FWHM, μm)
0.4-1.0	1-32	32	15-30
1.5-1.8	33-40	8	45
2.0-2.5	41-72	32	20
3.0-5.0	73	1	2
8.0-12.6	74-79	6	0.9
TIR bands:			
8.75	74		
9.65	75		
10.48	76		
11.27	77		
12.00	78		
12.67	79		

TABLE III
AHS SPECTRAL CHARACTERISTICS. VALUES OF EFFECTIVE WAVELENGTH FOR TIR BANDS ARE ALSO GIVEN

Wavelength Range (μm)	Bands	Number of Bands	Band-Width (FWHM, μm)
0.441-1.018	1-20	20	0.03
1.491-1.650	21	1	0.2
2.019-2.448	22-63	42	0.013
3.03-5.41	64-70	7	0.3
7.95-13.17	71-80	10	0.4-0.5
TIR bands:			
8.18	71		
8.66	72		
9.15	73		
9.60	74		
10.07	75		
10.59	76		
11.18	77		
11.78	78		
12.35	79		
12.93	80		

the VNIR (32 bands), SWIR (8 + 32 bands), Mid IR (MIR) (one band), and TIR (six bands) spectral ranges. The DAIS scan mechanism is a Kennedy type, with an Instantaneous Field of View (IFOV) of 3.3 mrad and a FOV of $\pm 26^{\circ}$. Spectral characteristics of the DAIS sensor are given in Table II.

The AHS sensor was developed by SensyTech Inc. (currently ArgonST, USA), and it is operated by the Spanish Institute of Aeronautics onboard its aircraft CASA 212–200 Paternina. It has 80 spectral bands covering the VNIR (20 bands), SWIR (1 + 42 bands), MIR (seven bands), and TIR (ten bands). The optical design is composed by a scan mirror plus Cassegrain-type afocal telescope with a single IFOV determining field stop (Pfund assembly). AHS has an IFOV of 2.5 mrad and a FOV of $\pm 45^{\circ}$. Spectral characteristics are summarized in Table III.

C. Field Campaigns and Laboratory Measurements

Field measurements, and most of the imagery included in this paper, were collected in the framework of field campaigns carried out over different areas. We provide, in this section, a brief explanation of the different field campaigns and test areas.

The European Space Agency carries out a number of airborne campaigns to support geophysical-algorithm development, calibration/validation, and the simulation of future space-borne Earth-observation missions. The DAIS experiments were

performed in 1998, 1999, and 2000 (DAISEX-1998, DAISEX-1999, and DAISEX-2000), the SPECTRA Barrax Campaign conducted in 2003 and 2004 (SPARC-2003 and SPARC-2004), and the Sentinel-2 and Fluorescence Experiment performed in 2005 (SEN2FLEX-2005) are samples of these campaigns. All these field campaigns were carried out in the Barrax test site, situated in the west of the province of Albacete (Spain), 28 km from the capital town (39°3′ N, 2°6′ W, 700 m). The land use in the 10 000-ha area is approximately 65% dry land (of which 67% are winter cereals and 33% fallow land) and 35% irrigated land (corn 75%; barley/sunflower 15%; alfalfa 5%; onions 2.9%; and vegetables 2.1%). The Barrax area includes three agro-meteorological stations [26].

An intensive series of field experiments were conducted in Morocco from March 3–17, 2003. This field experiment was included in the WATer-use Efficiency in natural vegetation and agricultural areas by Remote sensing in the MEDiterranean basin project, whose description is given by [27]. Measurements of emissivity and surface radiometric temperature were carried out concurrently with the AATSR overpass. The study area where the experimental field campaign took place was located between 31°39′ and 31°41′ N latitude and between 7°33′ and 7°38′ W longitude, on the River Tensift basin in the east of Marrakech (Morocco), 600 m above sea level [28].

The instrumentation involved in the field measurements included single-band (RAYTEK ST6, RAYTEK Thermalert MID, and OPTRIS MiniSight Plus) and multiband (CIMEL models CE-312-1 and CE-312-2) thermal radiometers. Among these instruments, the CIMEL model CE-312-2 is remarkable for its similarity with the ASTER TIR bands, which allows the application of the TES algorithm for recovering surface emissivities from ground-based measurements, as discussed in Section II-C. Fig. 1 shows the filter functions of the CIMEL bands. Calibration sources (black bodies, EVEREST model 1000, and GALAI model 204-P) were also used. A diffuse-reflectance standard plate (model Labsphere Infragold) was used to estimate the sky irradiance.

Samples of bare soil were collected in the Barrax area and also measured in the laboratory. A high-spectral-resolution emissivity spectrum was measured at the Jet Propulsion Laboratory (JPL) with the Nicolet spectrometer. Low spectral measurements were carried out with the CIMEL CE-312-2 instrument in the laboratory of the Global Change Unit (University of Valencia) [25].

IV. Results and Discussion

A. Application to VNIR Sensors With Low-Spectral TIR Capabilities: AVHRR, AATSR, SEVIRI, MODIS, and TM5

Sensors with one or two TIR bands, such as AVHRR, AATSR, or TM5, do not have the multispectral capabilities required to apply the TES algorithm, so only the $\mathrm{NDVI}^{\mathrm{THM}}$ can be applied. The same occurs with MODIS and SEVIRI sensors, since, despite that they have *a priori* TIR bands enough to apply the TES algorithm, not all of them are located in the proper TIR spectral region (TES algorithm requires at least four TIR bands located in atmospheric windows to provide satisfactory results).

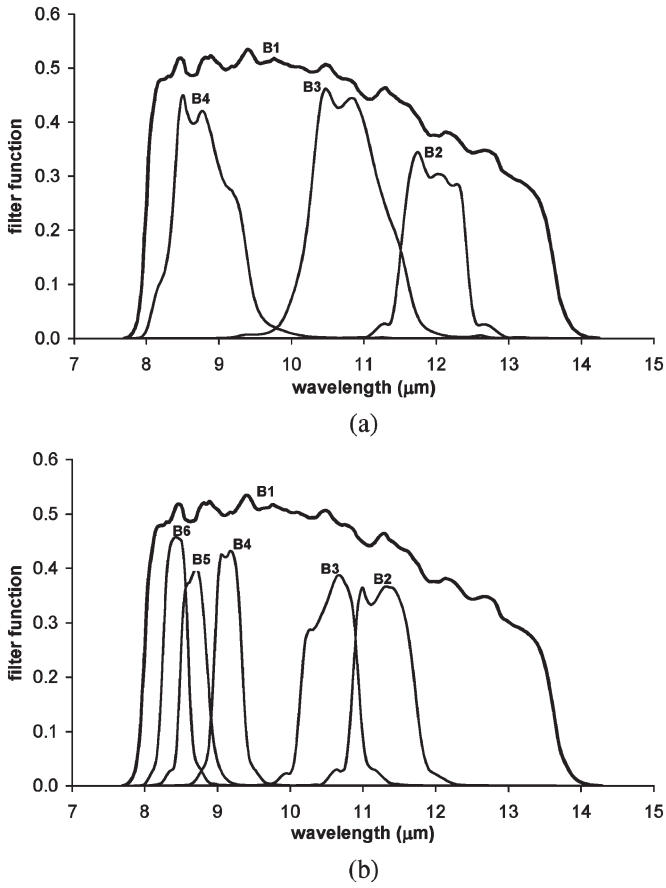

Fig. 1. Filter functions for the field radiometers. (a) CIMEL CE 312-1. (b) CIMEL CE 312-2.

The $\mathrm{NDVI}^{\mathrm{THM}}$ was first developed and applied to AVHRR data over a study area located in Morocco [13]. A comparison between $\mathrm{NDVI}^{\mathrm{THM}}$, TISI, and DNM applied to AVHRR data over the Iberian Peninsula was presented in [29], the $\mathrm{NDVI}^{\mathrm{THM}}$ providing similar results than the others. $\mathrm{NDVI}^{\mathrm{THM}}$ and AVHRR imagery included in the Pathfinder AVHRR Land database has also been used over the whole European continent [30]. The method was applied to MODIS data acquired over the Iberian Peninsula in [31], and it has been compared to the MODIS DNM algorithm by [32]. The conclusion of this last study is that the $\mathrm{NDVI}^{\mathrm{THM}}$ provides almost the same results than the ones derived from the MODIS DNM algorithm, being the first one easier to implement.

$\mathrm{NDVI}^{\mathrm{THM}}$ has been also adapted to AATSR and SEVIRI data, but no validation or intercomparison against other methods has been performed until now. The application of the $\mathrm{NDVI}^{\mathrm{THM}}$ to TM data acquired over the Requena–Utiel site (Valencia, Spain) was analyzed in [33], and the results were compared against *in situ* measurements using the box method. The root mean square error (rmse) obtained was below 0.01. $\mathrm{NDVI}^{\mathrm{THM}}$ has also been applied to TM data acquired over the Barrax area.

Table IV shows the different expressions involved in the $\mathrm{NDVI}^{\mathrm{THM}}$ that have been successfully applied to the previously mentioned operational sensors. Some of these expressions have been previously published, whereas others are presented in this paper for the first time.

TABLE IV
EXPRESSIONS FOR THE $NDVI^{THM}$ ADAPTED TO DIFFERENT OPERATIONAL SATELLITE SENSORS. FOR THOSE EQUATIONS PREVIOUSLY PUBLISHED, THE REFERENCE IS GIVEN IN SQUARE BRACKETS. IN THE CASE OF THE TM SENSOR, THE REFERENCE ONLY REFERS TO THE CASE $0.2 \leq NDVI \leq 0.5$

SENSOR	NDVI<0.2	0.2≤NDVI≤0.5	NDVI>0.5
AVHRR [13]	ε_4=0.979-0.057ρ_1	ε_4=0.968+0.021P_v	ε_4=0.99
	ε_5=0.982-0.028ρ_1	ε_5=0.974+0.015P_v	ε_5=0.99
AATSR	ε_{11}=0.981-0.061ρ_1	ε_{11}=0.970+0.012P_v	ε_{11}=0.99
	ε_{12}=0.985-0.042ρ_1	ε_{12}=0.977+0.008P_v	ε_{12}=0.99
SEVIRI	$\varepsilon_{8.7}$=0.985-0.291$\rho_{vis0.6}$	$\varepsilon_{8.7}$=0.931+0.059P_v	$\varepsilon_{8.7}$=0.99
	$\varepsilon_{9.7}$=0.974-0.155$\rho_{vis0.6}$	$\varepsilon_{9.7}$=0.945+0.046P_v	$\varepsilon_{9.7}$=0.99
	$\varepsilon_{10.8}$=0.977-0.048$\rho_{vis0.6}$	$\varepsilon_{10.8}$=0.968+0.021P_v	$\varepsilon_{10.8}$=0.99
	$\varepsilon_{12.0}$=0.981-0.026$\rho_{vis0.6}$	$\varepsilon_{12.0}$=0.976+0.015P_v	$\varepsilon_{12.0}$=0.99
	$\varepsilon_{13.4}$=0.986-0.040$\rho_{vis0.6}$	$\varepsilon_{13.4}$=0.978+0.014P_v	$\varepsilon_{13.4}$=0.99
MODIS [31]	ε_{31}=0.984-0.088ρ_1	ε_{31}=0.974+0.015P_v	ε_{31}=0.99
	ε_{32}=0.982-0.028ρ_1	ε_{32}=0.968+0.021P_v	ε_{32}=0.99
TM [33]	ε_{TM6}=0.979-0.035ρ_{TM3}	ε_{TM6}=0.986+0.004P_v	ε_{TM6}=0.99

B. Application to High-Spectral VNIR Sensors Without TIR Bands: CHRIS

Even when a certain sensor does not have TIR bands, land surface emissivity can be retrieved with the $NDVI^{THM}$ or $SNDVI^{THM}$, since they only require VNIR bands. The particularization to a TIR band is achieved when the different laboratory spectra used for estimation of soil and vegetation emissivities is averaged according to the considered TIR-band filter function. Let us to consider the simplified expression given by (5). If the cavity term is neglected, it is possible to estimate the surface emissivity in a very simple way

$$\varepsilon_\lambda = \varepsilon_{v\lambda} P_V + \varepsilon_{s\lambda} (1 - P_V). \tag{10}$$

Therefore, one can propose expressions of ε as a function of P_V for different TIR bands, but P_V can be estimated from other sensors. Note that (10) provides $\varepsilon = \varepsilon_s$ when $P_v = 0$ and $\varepsilon = \varepsilon_v$ when $P_V = 1$, which is precisely the $SNDVI^{THM}$ given by (9). However, P_V can be estimated from VNIR data using other methods than those based on NDVI estimations.

Taking advantage of the availability of two CHRIS images acquired during SPARC-2003 (July 12 and 14), which were atmospherically corrected and converted into reflectivities [34], we analyzed the accuracy of other methods for P_V retrieval, as well as the impact of the P_V accuracy on surface emissivity estimated from (10). The methods tested were the use of the Variable Atmospherically Resistant Index ($VARI_{green}$), as proposed by [35], and Spectral Mixture Analysis (SMA) techniques, such as the Linear Spectral Unmixing (LSU).

The $VARI_{green}$ was proposed to solve the saturation problems of the NDVI for high vegetation covers. This index is computed in a similar way to that of the NDVI, but using green and red reflectivities. It is designed to be obtained from top-of-atmosphere values, so it also includes the blue reflectivities to account for the atmospheric effects

$$VARI_{green} = \frac{\rho_{green} - \rho_{red}}{\rho_{green} + \rho_{red} - \rho_{blue}}. \tag{11}$$

A linear relation between P_V and $VARI_{green}$ was proposed in [35], $P_V = 0.8475\ VARI_{green} + 0.2278$, with a standard error of estimation of less than 10%. This equation was applied to CHRIS images and tested against seven *in situ* values of P_V obtained using an hemispherical digital camera over different crops (garlic, alfalfa, corn, sugarbeet, and potatoes, with P_V values ranging from 0.12 to 0.96, as it is shown in Table V) [36]. The results obtained were not satisfactory, with an underestimation in the P_V of 28%. This fact led us to find a new relation using *in situ* measurements. In this case, the following relation was obtained:

$$P_V = 1.1330 VARI_{green} + 0.4340 \tag{12}$$

with a correlation coefficient of $r = 0.97$ and a standard error of estimation of 8%. These results suggest that, despite the relation between P_V and $VARI_{green}$ is accurate enough, it could depend on the test site considered. For comparison, P_V was also retrieved using (7). Values of $NDVI_s = 0.11$ and $NDVI_v = 0.83$ were found from the NDVI histogram, and the test against the *in situ* values provided an rmse of 15% (see Table V).

SMA technique has been developed in recent years to extract land-cover information at a subpixels level. SMA divides each ground resolution element into its constituent materials using endmembers (EMs), which represent the spectral characteristics of the cover types. When applied to multispectral satellite data, the result is a series of images that each is depicting the abundance of a cover type [37]. In the case of CHRIS data, a simple linear-mixing model LSU has been

TABLE V
TEST OF DIFFERENT METHODS FOR PROPORTION OF VEGETATION (P_V) RETRIEVAL OVER THE AGRICULTURAL AREA OF BARRAX. P_V^{SITU} REFERS TO *IN SITU* MEASUREMENTS USING HEMISPHERICAL PHOTOGRAPHS, AND $NDVI^{CHRIS}$ IS THE NDVI EXTRACTED FROM THE PROBA–CHRIS IMAGE ACQUIRED AT NEAR-NADIR VIEW AND USING BANDS 48 (0.852 μm) AND 25 (0.674 μm). STANDARD DEVIATION IS GIVEN IN BRACKETS. METHODS TESTED ARE P_V^{NDVI}, IN WHICH P_V IS RETRIEVED FROM THE SCALED NDVI (7), $P_V^{LSU-AMEE}$, IN WHICH P_V IS RETRIEVED FROM A LINEAR SPECTRAL UNIMIXING USING THE AMEE METHOD TO EXTRACT THE EMS, AND $P_V^{LSU-MAP}$, WHICH USES THE LINEAR SPECTRAL UNMIXING USING THE LAND-USE MAP TO EXTRACT THE EMS. MEAN VALUE FOR THE DIFFERENCE BETWEEN P_V ESTIMATED WITH THE METHODS AND THE ONE MEASURE *IN SITU* (BIAS), WITH THE STANDARD DEVIATION (σ) AND THE RMSE ARE ALSO GIVEN

PLOT	P_V^{situ}	$NDVI^{CHRIS}$	P_V^{NDVI}	$P_V^{LSU-AMEE}$	$P_V^{LSU-MAP}$
Garlic	0.12 (0.09)	0.18 (0.02)	0.008	0.127	0.133
Alfalfa #1	0.59 (0.12)	0.67 (0.06)	0.598	0.622	0.588
Corn #1	0.63 (0.08)	0.80 (0.04)	0.917	0.861	0.782
Corn #2	0.71 (0.12)	0.792 (0.014)	0.898	0.818	0.775
Alfalfa #2	0.73 (0.12)	0.72 (0.05)	0.718	0.623	0.683
Sugar beet	0.923 (0.013)	0.791 (0.013)	0.894	0.901	0.816
Potatoes	0.96 (0.04)	0.80 (0.03)	0.913	1.062	0.880
		Bias:	0.04	0.05	0.00
		σ:	0.14	0.11	0.09
		RMSE:	0.15	0.12	0.09

TABLE VI
MEAN EFFECTIVE EMISSIVITIES FOR CIMEL 312-1 BANDS OBTAINED FROM THE ASTER SPECTRAL LIBRARY FOR EACH SOIL CLASS AND FOR VEGETATION. STANDARD-DEVIATION VALUES ARE GIVEN IN BRACKETS

CLASS	No.	B1	B2	B3	B4
Alfisol	9	0.950 (0.016)	0.976 (0.003)	0.967 (0.004)	0.91 (0.04)
Aridisol	14	0.959 (0.012)	0.974 (0.004)	0.969 (0.007)	0.94 (0.03)
Entisol	10	0.95 (0.02)	0.979 (0.002)	0.969 (0.006)	0.90 (0.06)
Inceptisol	7	0.962 (0.009)	0.976 (0.004)	0.969 (0.006)	0.946 (0.017)
Mollisol	9	0.966 (0.009)	0.978 (0.002)	0.972 (0.003)	0.95 (0.02)
All soils	**49**	**0.957 (0.016)**	**0.976 (0.004)**	**0.969 (0.006)**	**0.93 (0.04)**
Vegetation	3	0.983 (0.007)	0.984 (0.010)	0.982 (0.008)	0.982 (0.007)

TABLE VII
SAME AS TABLE VI BUT FOR THE CIMEL 312-2 BANDS. VALUES FOR BAND 1 ARE NOT SHOWN, SINCE THIS BAND IS THE SAME FOR BOTH CIMELS

CLASS	No.	B2	B3	B4	B5	B6
Alfisol	9	0.969 (0.003)	0.966 (0.005)	0.91 (0.04)	0.91 (0.04)	0.92 (0.05)
Aridisol	14	0.970 (0.005)	0.968 (0.007)	0.94 (0.03)	0.94 (0.03)	0.93 (0.03)
Entisol	10	0.973 (0.004)	0.968 (0.007)	0.90 (0.06)	0.89 (0.07)	0.89 (0.06)
Inceptisol	7	0.970 (0.006)	0.968 (0.006)	0.94 (0.02)	0.949 (0.016)	0.946 (0.016)
Mollisol	9	0.973 (0.003)	0.972 (0.003)	0.95 (0.02)	0.95 (0.02)	0.95 (0.02)
All soils	**49**	**0.971 (0.005)**	**0.968 (0.006)**	**0.93 (0.04)**	**0.93 (0.05)**	**0.93 (0.04)**
Vegetation	3	0.983 (0.009)	0.981 (0.007)	0.979 (0.010)	0.982 (0.007)	0.986 (0.006)

used, in which only a few EMs are used to describe the surface composition in each pixel of an image [38]. The reflectivity spectra for each EM have been automatically extracted from the image using the Automated Morphological Endmember Extraction (AMEE) method [39], [40]. The AMEE method extracted a total amount of ten EMs identified as vegetation, clouds, bare soil, shadows, etc. $P_{\rm V}$ values were extracted from the abundance of the EM corresponding to vegetation (highest NDVI). The test against *in situ* measurements provided an rmse $= 12\%$ (Table V). It is also possible to select the EMs using a land-cover map of the test site. For this purpose, we selected only two EMs, corresponding to bare soil ($P_{\rm V} = 0$) and potatoes ($P_{\rm V} \sim 1$). In this way, the results are slightly better, with an rmse $= 9\%$ according to the results presented in Table V. The main constraint, in this case, is that *a priori* knowledge of the field site is needed in order to extract the EMs.

Once the $P_{\rm V}$ was retrieved from CHRIS VNIR data, land surface emissivity maps were obtained from CHRIS images using (10). For this purpose, different soil and vegetation spectra extracted from the ASTER spectral library [41] were considered. These spectra were averaged using the filter functions corresponding to the CIMEL 312-1 and 312-2 instruments described in Section III-C. Reasons for selecting CIMEL instruments are the following: 1) these instruments are used for field measurements, so emissivity maps particularized to CIMEL bands could be used as a kind of *in situ* maps instead of disperse emissivity measurements achieved with the box or TES algorithm and 2) the five CIMEL 312-2 narrow bands are in coincidence with the five TIR ASTER bands (CIMEL 312-2 bands 6, 5, 4, 3, and 2 are equivalent to ASTER bands 10, 11, 12, 13, and 14, with effective wavelengths of 8.43, 8.69, 9.15, 10.57, and 11.29 μm, respectively), and CIMEL 312-1 bands 3 (10.80 μm) and 2 (11.96 μm) are very similar to AVHRR bands 4 (10.79 μm) and 5 (12.00 μm), respectively, so these emissivity maps could be also used to compare values extracted from ASTER or AVHRR imagery. Tables VI and VII show mean emissivity values for different soils and vegetation samples particularized to CIMEL 312-1 and 312-2 bands. When all the soils are considered, standard-deviation values for bands located in the region between 8 and 9.5 μm are extremely high (> 0.04), which indicates that a mean standard value for soil cannot be considered in this spectral region. For this reason, only the Inceptisol class has been considered in order to adapt (10) to the CIMEL bands. This class show acceptable standard-deviation values (< 0.02) in 8–9.5 μm, and it is the more common soil class on the Earth's surface. Therefore, when a mean emissivity value for the Inceptisol class and a mean value for the vegetation samples are considered, it is possible to obtain the expressions included in Table VIII for ε retrieval from $P_{\rm V}$ values. As an example, Fig. 2 shows land surface emissivity maps obtained for the CIMEL 312-2 bands using the $P_{\rm V}$ image obtained from CHRIS data with the LSU technique.

TABLE VIII
EXPRESSIONS FOR THE LAND SURFACE EMISSIVITY RETRIEVAL FROM FVC ($P_{\rm V}$) VALUES ADAPTED TO EACH CIMEL BAND. IN BOTH CASES, BAND 1 REFERS TO A BROAD BAND CHANNEL (8–14 μm)

INSTRUMENT	BAND	EXPRESSION
CIMEL 312-1	1 (10.54 μm)	$\varepsilon = 0.962 + 0.021\ P_v$
	2 (11.96 μm)	$\varepsilon = 0.976 + 0.008\ P_v$
	3 (10.80 μm)	$\varepsilon = 0.969 + 0.013\ P_v$
	4 (8.82 μm)	$\varepsilon = 0.946 + 0.036\ P_v$
CIMEL 312-2	1 (10.54 μm)	$\varepsilon = 0.962 + 0.021\ P_v$
	2 (11.29 μm)	$\varepsilon = 0.970 + 0.013\ P_v$
	3 (10.57 μm)	$\varepsilon = 0.968 + 0.013\ P_v$
	4 (9.15 μm)	$\varepsilon = 0.941 + 0.038\ P_v$
	5 (8.69 μm)	$\varepsilon = 0.949 + 0.033\ P_v$
	6 (8.43 μm)	$\varepsilon = 0.946 + 0.040\ P_v$

It should be noted that, according to the sensitivity analysis presented in [42], the error on emissivity due to the error on $P_{\rm V}$, $e(P_V)$, when using (10) is given by the term $(\varepsilon_{\rm v}–\varepsilon_{\rm s})\ e(P_{\rm V})$. For example, considering CIMEL 312-2 band 4 (Table VII), the difference between $\varepsilon_{\rm v}$ and $\varepsilon_{\rm s}$ for Inceptisols is 0.04. An error of 0.15 in $P_{\rm V}$, as is the case when using the scaled NDVI, contributes to the error on ε in 0.006, whereas an error of 0.10 in $P_{\rm V}$, as is approximately the case of the LSU, contributes in 0.004. Both quantities are similar and reasonably accepted as low errors on emissivity, so despite that, LSU techniques are expected to provide more accurate values than those based on NDVI, both methods are accurate enough to apply the simple expression given by (10).

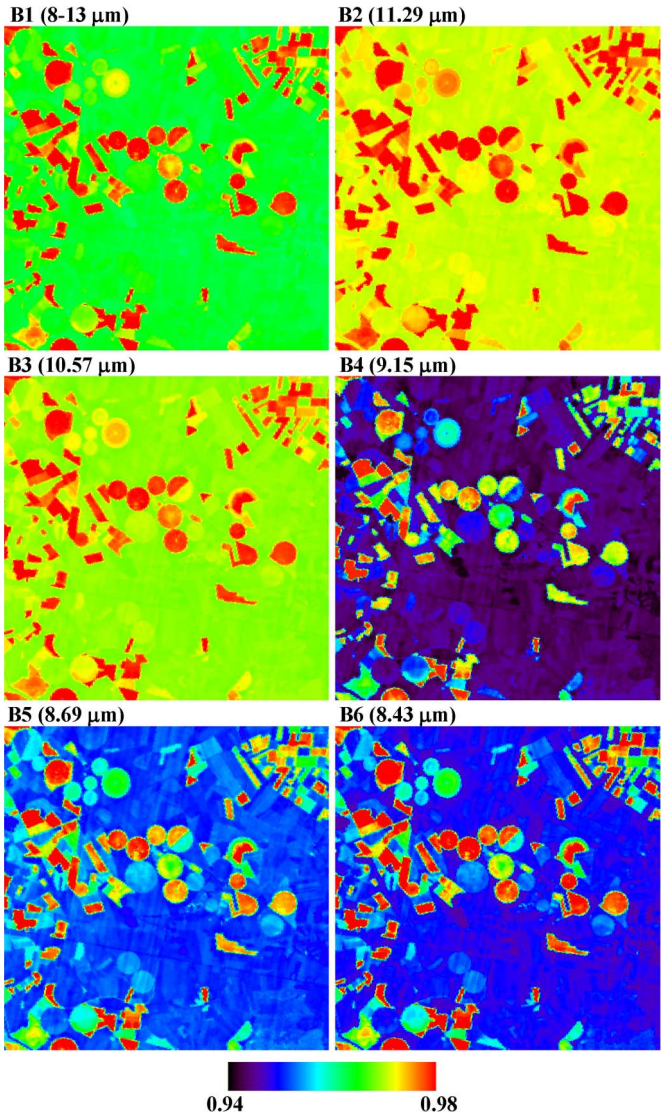

Fig. 2. Land surface emissivity maps obtained from CHRIS data over the Barrax test site for the six CIMEL 312-2 thermal bands.

C. Application to VNIR Sensors With Multispectral TIR Capabilities: Comparison Between TES and NDVI$^{\mathrm{THM}}$ From ASTER Data

Both NDVI$^{\mathrm{THM}}$ and TES methods can be applied to sensors with VNIR and multispectral TIR bands. This is the case of ASTER, with three bands in the VNIR region and five TIR bands, all of them located in atmospheric windows, as presented in Section III-A. The existence of a sensor with the characteristics required to apply NDVI$^{\mathrm{THM}}$ and TES methods provides an excellent opportunity to compare the two methods, since they are applied to the same data under the same conditions. This analysis was carried out using five ASTER images acquired in 2000 and 2001 over the Barrax test site, which included two ASTER Level-2 standard products: at surface VNIR reflectivities (AST-07) used to predict ε from NDVI, and surface emissivities (AST-05) produced with the TES algorithm. A detailed analysis of the results obtained is presented in [14]. In short, emissivities from VNIR data were estimated using the SNDVI$^{\mathrm{THM}}$ discussed in Section II-B [(9)]. Values for ε_{s} were extracted from mean values of different samples included in the Inceptisol class (see values given in Table VII), and a constant value for ε_{v} of 0.99 was considered, thus leading to the following expressions for ASTER TIR bands from 10 to 14:

$$\begin{aligned}\varepsilon_{10} &= 0.946 + 0.044P_{\mathrm{V}}\\ \varepsilon_{11} &= 0.949 + 0.041P_{\mathrm{V}}\\ \varepsilon_{12} &= 0.941 + 0.049P_{\mathrm{V}}\\ \varepsilon_{13} &= 0.968 + 0.022P_{\mathrm{V}}\\ \varepsilon_{14} &= 0.970 + 0.020P_{\mathrm{V}}.\end{aligned} \tag{13}$$

$\mathrm{NDVI_v}$ and $\mathrm{NDVI_s}$ values needed to estimate $\mathrm{P_v}$ from (7) were extracted from the NDVI histogram. Emissivities extracted from ASTER images over fully vegetated areas (corn) and bare soil were tested against values retrieved from ground-based measurements using the CIMEL 312-2 and the TES algorithm. The SNDVI$^{\mathrm{THM}}$ provided rmse values lower than 0.005 for fully vegetated areas and lower than 0.015 for bare soil, and the TES method provided an rmse (0.01 over fully vegetated areas, but rmse > 0.03 for bare soil). These results were obtained because the accuracy of the TES is expected to decrease for surface with low spectral contrast, as is the case of agricultural areas, such as the Barrax site. However, the TES algorithm is *a priori* applicable to any kind of natural surfaces, providing also surface temperatures and with accurate results over surface of high spectral contrast. Fig. 3 shows an example of the ASTER emissivity maps obtained with the NDVI and TES methods over Barrax. Note that ε from NDVI values show higher resolution, since ASTER VNIR bands provide a pixel size of 15 m versus the 90 m of the TIR bands. Noisy appearance in the TES images are attributed to the scaling problem discussed in [14]–[16].

D. Adaptation to Airborne Sensors: DAIS and AHS

NDVI$^{\mathrm{THM}}$ and TES methods were adapted to DAIS and AHS airborne-sensor characteristics. In the case of DAIS, NDVI$^{\mathrm{THM}}$, TES, and NEM methods were compared from imagery acquired over the Barrax area in the framework of the DAISEX campaigns [43]. NDVI$^{\mathrm{THM}}$ was applied using the following expressions:

$$\mathrm{NDVI} < 0.2, \quad \begin{bmatrix}\varepsilon_{74}\\ \varepsilon_{75}\\ \varepsilon_{76}\\ \varepsilon_{77}\\ \varepsilon_{78}\\ \varepsilon_{79}\end{bmatrix} = \begin{bmatrix}-0.378\\ -0.209\\ -0.094\\ -0.081\\ -0.063\\ -0.066\end{bmatrix}\rho_{10} + \begin{bmatrix}1.002\\ 0.986\\ 0.984\\ 0.988\\ 0.988\\ 0.991\end{bmatrix} \tag{14}$$

$$0.2 \le \mathrm{NDVI} \le 0.5, \quad \begin{bmatrix}\varepsilon_{74}\\ \varepsilon_{75}\\ \varepsilon_{76}\\ \varepsilon_{77}\\ \varepsilon_{78}\\ \varepsilon_{79}\end{bmatrix} = \begin{bmatrix}0.963\\ 0.972\\ 0.982\\ 0.985\\ 0.987\\ 0.988\end{bmatrix} + \begin{bmatrix}0.025\\ 0.016\\ 0.008\\ 0.006\\ 0.004\\ 0.002\end{bmatrix} P_V \tag{15}$$

$$\mathrm{NDVI} > 0.5, \quad \varepsilon_{74} = \varepsilon_{75} = \varepsilon_{76} = \varepsilon_{77} = \varepsilon_{78} = \varepsilon_{79} = 0.99 \tag{16}$$

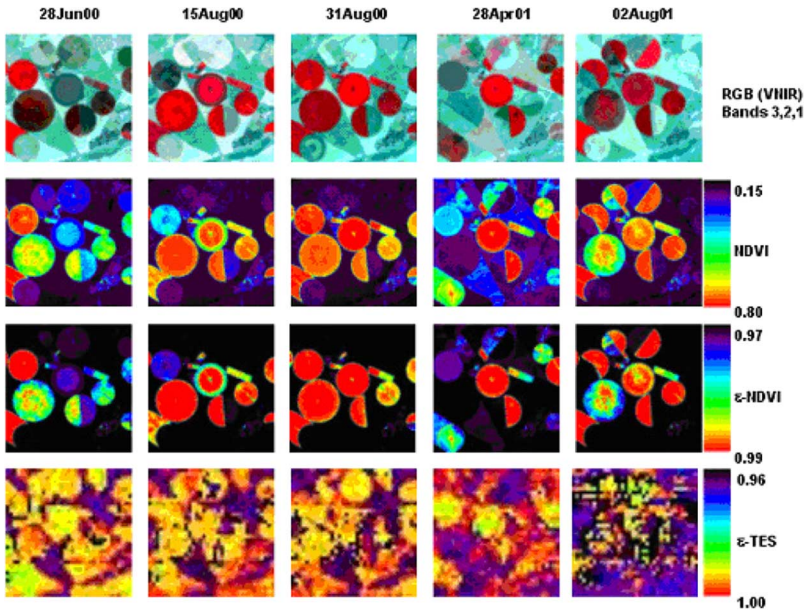

Fig. 3. Emissivity imagery obtained from ASTER data over the Barrax test site in 2000 and 2001, using the SNDIV$^{\mathrm{THM}}$ (ε-NDVI) and the TES (ε-TES) methods. RGB composites and NDVI are also displayed. Emissivity images correspond to ASTER TIR band 13 (10.66 μm).

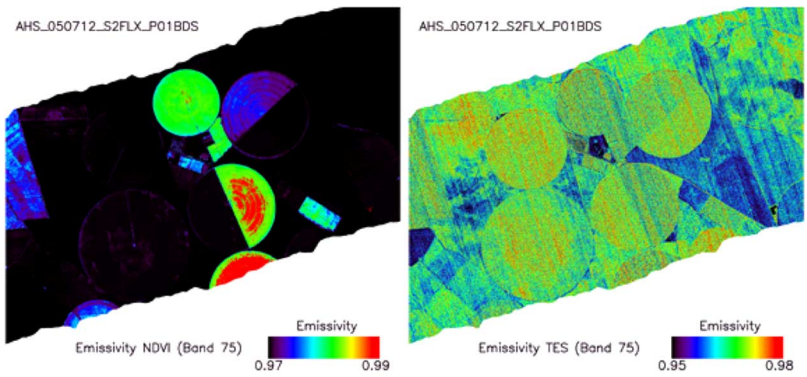

Fig. 4. Land surface emissivity maps obtained from AHS band 75 (10.06 μm) using (left) the SNDVI$^{\mathrm{THM}}$ and (right) TES methods. AHS images were acquired on July 12, 2006 at 11:56 GMT over the Barrax area in the framework of the SEN2FLEX campaign. Pixel size is 2 m.

where ρ_{10} refers to DAIS band 10 (0.659 μm) located in the red region. DAIS bands from 74 to 79 refer to the TIR bands included in Table II. TES algorithm was adapted to DAIS characteristics by finding a new relation between minimum emissivity ($\varepsilon_{\min}$) and spectral contrast (MMD)

$$\varepsilon_{\min} = 0.984 - 1.062\mathrm{MMD}. \tag{17}$$

The comparison presented in [43] showed that differences between NDVI$^{\mathrm{THM}}$, TES, and NEM range from 1% to 2%, where NDVI$^{\mathrm{THM}}$ provides the best results for vegetated plots and NEM provides the best results over bare soils. For this reason, a hybrid method was proposed, using NEM when NDVI < 0.2 and NDVI$^{\mathrm{THM}}$ when $0.2 \leq$ NDVI ≤ 0.5 (a constant value of 0.99 was maintained for NDVI > 0.5).

The SNDVI$^{\mathrm{THM}}$ has been applied to AHS data acquired in the framework of the SEN2FLEX campaigns carried out in Barrax [44]. For this purpose, the soil emissivities were extracted from the ε spectrum measured at the JPL with the Nicolet Spectrometer [45] from one sample of bare soil collected at the Barrax area. The expressions obtained are the following:

$$\begin{bmatrix} \varepsilon_{71} \\ \varepsilon_{72} \\ \varepsilon_{73} \\ \varepsilon_{74} \\ \varepsilon_{75} \\ \varepsilon_{76} \\ \varepsilon_{77} \\ \varepsilon_{78} \\ \varepsilon_{79} \\ \varepsilon_{80} \end{bmatrix} = \begin{bmatrix} 0.945 \\ 0.967 \\ 0.971 \\ 0.969 \\ 0.974 \\ 0.979 \\ 0.980 \\ 0.981 \\ 0.985 \\ 0.985 \end{bmatrix} + \begin{bmatrix} 0.045 \\ 0.023 \\ 0.019 \\ 0.021 \\ 0.016 \\ 0.011 \\ 0.010 \\ 0.009 \\ 0.005 \\ 0.005 \end{bmatrix} P_V \tag{18}$$

where AHS bands from 71 to 80 refer to the TIR bands included in Table III.

Fig. 4 shows some examples of land surface emissivity maps obtained from AHS data with the SNDVI$^{\mathrm{THM}}$ and TES algorithms over the Barrax area. Similarly to the maps presented in Fig. 3 from ASTER data, TES images show again a noisy

appearance. Land-surface temperature results from AHS have been tested against *in situ* measurements in [44] and [46], but no validation have been carried out with emissivity results until now.

The feasibility of applying the $\mathrm{NDVI}^{\mathrm{THM}}$ to AHS data is also explored in this section, albeit the discussion is presented in terms of simulated data. We have focused on the case when $\mathrm{NDVI} < \mathrm{NDVI_s}$, which is a critical point on the method, since not all the soils seem to provide a good correlation between ε and ρ [32]. $\mathrm{NDVI}^{\mathrm{THM}}$ was first developed for low-spectral-resolution sensors, so only one band located in the red region was considered at first. However, one can consider linear combinations between all the bands located in the VNIR region. Hence, in the case of AHS with bands from 1 to 20 located in the VNIR, emissivities for pixels with $\mathrm{NDVI} < \mathrm{NDVI_s}$ could be estimated as

$$\varepsilon_i = a_i^{(0)} + \sum_{k=1}^{20} a_i^{(k)} \rho_k \tag{19}$$

where the subindex "i" refers to a certain AHS thermal band ($i = 71$ and 80). Table IX shows the correlation coefficients, and the standard errors of estimation corresponding to the statistical fits when only AHS band 9 (red) is considered or when the 20 AHS VNIR bands (19) are considered. The results have been obtained with a total amount of 38 soil samples extracted from the ASTER spectral library. It should be noted that, when an extensive dataset of soil emissivities is considered, correlations are very low, and error for bands located in the 8–9.5-μm region (bands from 71 to 74) are not satisfactory (σ from 0.02 to 0.04). However, errors for bands located in the 10–13-μm region (from 75 to 80) are acceptable ($\sigma < 0.01$). Both the correlation and the errors are significantly improved when considering (19), with σ ranging between 0.011 and 0.018 for bands 71–74 and 0.002 and 0.006 for bands 75–80. These preliminary results suggest that $\mathrm{NDVI}^{\mathrm{THM}}$ could be improved by exploitation of multispectral VNIR capabilities, particularly for emissivity retrieval from bands located in the 8–9.5-μm region, in which surface emissivities show higher variations and low correlations with only one band located in the red region.

TABLE IX
CORRELATION COEFFICIENTS (R) AND STANDARD ERRORS OF ESTIMATION (σ) OBTAINED FOR THE RELATIONS BETWEEN AHS EMISSIVITIES AT TIR BANDS 71–80, AND RED REFLECTIVITY (BAND 9), AND ALSO BETWEEN EMISSIVITIES AND LINEAR COMBINATIONS CONSTRUCTED WITH THE 20 AHS VNIR BANDS

	$\varepsilon_\lambda = a_\lambda + b_\lambda \rho_9$		$\varepsilon_\lambda = a_\lambda + \sum_{i=1}^{20} b_{\lambda,i} \rho_i$	
AHS BAND	r	σ	r	σ
71	0.105	0.033	0.837	0.018
72	0.366	0.041	0.905	0.018
73	0.106	0.035	0.859	0.018
74	0.043	0.020	0.836	0.011
75	0.043	0.011	0.807	0.006
76	0.168	0.006	0.804	0.003
77	0.231	0.005	0.778	0.003
78	0.170	0.005	0.750	0.003
79	0.034	0.003	0.760	0.002
80	0.101	0.007	0.811	0.004

V. CONCLUSION

Knowledge of surface emissivities from remote-sensing data has two major interests: 1) as an input for accurate land-surface-temperature estimates, particularly for low-resolution sensors and 2) for terrestrial and planetary geologic studies, for example, for mineral mapping [1], which can be only dealt from multispectral/hyperspectral thermal data.

Land surface emissivity retrieval from satellite/airborne sensors can be achieved using methods based on FVC estimations, such as $\mathrm{NDVI}^{\mathrm{THM}}$ or its simplified form $\mathrm{SNDVI}^{\mathrm{THM}}$, and also using methods that require multispectral TIR capabilities to solve the coupling between emissivity and temperature, as, for example, the TES algorithm. Despite that other methods have been published, the ones presented in this paper recover the absolute surface emissivity and they avoid the use of nighttime acquisitions.

The main advantages of the $\mathrm{NDVI}^{\mathrm{THM}}$ are as follows: 1) an accurate atmospheric correction is not needed when using a scaled NDVI for estimation of the FVC and the NDVI histogram for finding the NDVI thresholds (atmospheric correction is required when estimating soil emissivity from red reflectivity); 2) it can be applied to sensors with only one TIR band or even to sensors without TIR bands; and 3) higher resolution emissivity maps can be obtained for sensors in which the VNIR bands have higher spatial resolution than TIR bands. The problems involved in the $\mathrm{NDVI}^{\mathrm{THM}}$ are that the knowledge of soil emissivities are required in some cases and that it cannot be applied to certain surfaces such as water, snow, ice, and rocks. Some problems have also been found in the relation between soil emissivities for bands located in the 8–9.5-μm region and red reflectivities, which could be solved using multispectral VNIR bands instead of using only one VNIR band located in the red region. Applications for mineral mapping with very high spatial resolution data are also limited, since the method assumes that the surface is composed of soil and vegetation. It is also recommended to recalculate the NDVI thresholds for each site (for example, using the NDVI histogram), although global values of 0.2 for soil and 0.5 for vegetation could be chosen, as proposed in [13]. Over agricultural areas, higher NDVI values for vegetation can been found, which is around 0.8.

The main advantages of the TES algorithm are as follows: 1) it provides surface temperature and emissivity, simultaneously, and 2) it is *a priori* applicable to any kind of natural surface (also applicable to high spatial resolution data for mineral mapping). On the contrary, the main disadvantages are as follows: 1) an accurate atmospheric correction is needed and 2) some problems have been found due to the classification between pixels of low or high spectral contrast, which causes artifactual discontinuities on the emissivity products. TES algorithm cannot be applied to most operational sensors, since it requires at least four TIR bands located in atmospheric windows.

Taking into account the advantages and disadvantages of each method, a hybrid method could be developed to provide accurate land surface emissivity products.

REFERENCES

[1] R. G. Vaughan, W. M. Calvin, and J. V. Taranik, "SEBASS hyperspectral thermal infrared data: Surface emissivity measurements and mineral mapping," *Remote Sens. Environ.*, vol. 85, no. 1, pp. 48–63, Apr. 2003.

[2] P. S. Kealy and S. J. Hook, "Separating temperature and emissivity in thermal infrared multispectral scanner data: Implication for recovering land surface temperatures," *IEEE Trans. Geosci. Remote Sens.*, vol. 31, no. 6, pp. 1155–1164, Nov. 1993.

[3] K. Goïta and A. Royer, "Surface temperature and emissivity separability over land surface from combined TIR and SWIR AVHRR data," *IEEE Trans. Geosci. Remote Sens.*, vol. 35, no. 3, pp. 718–733, May 1997.

[4] S. Jaggi, D. Quattrochi, and R. Baskin, "An algorithm for the estimation of bounds on the emissivity and temperatures from thermal multispectral airborne remotely sensed data," in *Proc. Summary 3rd Annu. JPL Airborne Geosci. Workshop*, Pasadena, CA, 1992, pp. 22–24.

[5] A. Barducci and I. Pippi, "Temperature and emissivity retrieval from remotely sensed images using the grey body emissivity method," *IEEE Trans. Geosci. Remote Sens.*, vol. 34, no. 3, pp. 681–695, May 1996.

[6] T. Matsunaga, "A temperature–emissivity separation method using an empirical relationship between the mean, the maximum, and the minimum of the thermal infrared emissivity spectrum," *J. Remote Sens. Soc. Jpn.*, vol. 14, no. 2, pp. 230–241, 1994. in Japanese with English abstract.

[7] A. B. Kahle, D. P. Madura, and J. M. Soha, "Middle infrared multispectral aircraft scanner data: Analysis for geological applications," *Appl. Opt.*, vol. 19, no. 14, pp. 2279–2290, Jul. 1980.

[8] A. R. Gillespie, "Lithologic mapping of silicate rocks using TIMS," in *Proc. TIMS Data Users' Workshop*, Berkeley, CA, 1985, pp. 29–44.

[9] K. Watson, "Spectral ratio method for measuring emissivity," *Remote Sens. Environ.*, vol. 42, no. 2, pp. 113–116, Nov. 1992.

[10] F. Becker and Z.-L. Li, "Temperature-independent spectral indices in thermal infrared bands," *Remote Sens. Environ.*, vol. 32, no. 1, pp. 17–33, Apr. 1990.

[11] W. C. Snyder and Z. Wan, "BRDF models to predict spectral reflectance and emissivity in the thermal infrared," *IEEE Trans. Geosci. Remote Sen.*, vol. 36, no. 1, pp. 214–225, Jan. 1998.

[12] A. Gillespie, S. Rokugawa, T. Matsunaga, J. S. Cothern, S. Hook, and A. B. Kahle, "A temperature and emissivity separation algorithm for Advanced Spaceborne Thermal Emission and Reflection Radiometer (ASTER) images," *IEEE Trans. Geosci. Remote Sen.*, vol. 36, no. 4, pp. 1113–1126, Jul. 1998.

[13] J. A. Sobrino and N. Raissouni, "Toward remote sensing methods for land cover dynamic monitoring: Application to Morocco," *Int. J. Remote Sens.*, vol. 21, no. 2, pp. 353–366, Jan. 2000.

[14] J. C. Jiménez-Muñoz, J. A. Sobrino, A. Gillespie, D. Sabol, and W. T. Gustafson, "Improved land surface emissivities over agricultural areas using ASTER NDVI," *Remote Sens. Environ.*, vol. 103, no. 4, pp. 474–487, Aug. 2006.

[15] J. A. Sobrino, J. C. Jiménez-Muñoz, L. Balick, A. Gillespie, D. Sabol, and W. T. Gustafson, "Accuracy of ASTER Level-2 thermal-infrared standard products of an agricultural area in Spain," *Remote Sens. Environ.*, vol. 106, no. 2, pp. 146–153, Jan. 2007.

[16] W. T. Gustafson, A. R. Gillespie, and G. Yamada, "Revisions to the ASTER temperature/emissivity separation algorithm," in *Proc. 2nd Recent Advances Quantitative Remote Sens.*, Valencia, Spain, 2006, pp. 770–775.

[17] A. A. Van de Griend and M. Owe, "On the relationship between thermal emissivity and the normalized difference vegetation index for natural surfaces," *Int. J. Remote Sens.*, vol. 14, no. 6, pp. 1119–1131, 1993.

[18] E. Valor and V. Caselles, "Mapping land surface emissivity from NDVI: Application to European, African and South American areas," *Remote Sens. Environ.*, vol. 57, no. 3, pp. 167–184, Sep. 1996.

[19] J. A. Sobrino, V. Caselles, and F. Becker, "Significance of the remotely sensed thermal infrared measurements obtained over a citrus orchard," *ISPRS J. Photogramm. Remote Sens.*, vol. 44, pp. 343–354, 1990.

[20] T. N. Carlson and D. A. Ripley, "On the relation between NDVI, fractional vegetation cover, and leaf area index," *Remote Sens. Environ.*, vol. 62, no. 3, pp. 241–252, Dec. 1997.

[21] J. W. Salisbury and M. D'Aria, "Emissivity of terrestrial materials in the 8–14 μm atmospheric window," *Remote Sens. Environ.*, vol. 42, no. 2, pp. 83–106, Nov. 1992.

[22] J. W. Salisbury, A. Wald, and D. M. D'Aria, "Thermal-infrared remote sensing and Kirchhoff's law 1. Laboratory measurements," *J. Geophys. Res.*, vol. 99, no. B6, pp. 11897–11911, 1994.

[23] F. Nerry and M. P. Stoll, "Spectral properties of land surfaces in the thermal infrared. Part II: Field method for spectrally averaged emissivity measurements," *J. Geophys. Res.*, vol. 95, no. B5, pp. 7045–7062, 1990.

[24] V. Payan and A. Royer, "Analysis of temperature emissivity separation (TES) algorithm applicability and sensitivity," *Int. J. Remote Sens.*, vol. 25, no. 1, pp. 15–37, Jan. 2004.

[25] J. C. Jiménez-Muñoz and J. A. Sobrino, "Emissitivity spectra obtained from field and laboratory measurements using the temperature and emissivity separation algorithm," *Appl. Opt.*, vol. 45, no. 27, pp. 7104–7109, Sep. 2006.

[26] J. Moreno, V. Caselles, J. A. Martínez-Lozano, J. Meliá, J. A. Sobrino, A. Calera, F. Montero, and J. M. Cisneros, "The measurements programme at barrax," in *Proc. DAISEX Final Results Workshop*, Holland, The Netherlands, 2001, pp. 43–51.

[27] J. A. Sobrino, N. Raissouni, A. Olioso, C. B. Hasager, M. Ait Belaid, S. Abdel Rahman, and A. Chehbouni, "WATERMED—WATer use Efficiency in natural vegetation and agricultural areas by Remote sensing in the MEDiterranean basin," in *Proc IGARSS*, Sydney, Australia, 2001, pp. 9–13.

[28] G. Sòria and J. A. Sobrino, "ENVISAT/AATSR derived land surface temperature over a heterogeneous region," *Remote Sens. Environ*. DOI:10.1016/j.rse.2007.03.017, in press.

[29] J. A. Sobrino, N. Raissouni, and Z.-L. Li "A comparative study of land surface emissivity retrieval from NOAA data," *Remote Sens. Environ.*, vol. 75, no. 2, pp. 256–266, Feb. 2001.

[30] Y. Julien, J. A. Sobrino, and W. Verhoef, "Changes in land surface temperatures and NDVI values over Europe between 1982 and 1999," *Remote Sens. Environ.*, vol. 103, no. 1, pp. 43–55, Jul. 2006.

[31] J. A. Sobrino, J. El Kharraz, and Z.-L. Li, "Surface temperature and water vapour retrieval from MODIS data," *Int. J. Remote Sens.*, vol. 24, no. 24, pp. 5161–5182, Dec. 2003.

[32] M. Momeni and M. R. Saradjian, "Evaluating NDVI-based emissivities of MODIS bands 31 and 32 using emissivities derived by day/night LST algorithm," *Remote Sens. Environ.*, vol. 106, no. 2, pp. 190–198, Jan. 2007.

[33] J. A. Sobrino, J. C. Jiménez-Muñoz, and L. Paolini, "Land surface temperature retrieval from LANDSAT TM 5," *Remote Sens. Environ.*, vol. 90, no. 4, pp. 434–440, Apr. 2004.

[34] L. Guanter, L. Alonso, and J. Moreno, "A method for the surface reflectance retrieval from PROBA/CHRIS data over land: Application to ESA SPARC campaigns," *IEEE Trans. Geosci. Remote Sens.*, vol. 43, no. 12, pp. 2908–2917, Dec. 2005.

[35] A. A. Gitelson, Y. J. Kaufman, R. Stark, and D. Rundquist, "Novel algorithms for remote sensing estimation of vegetation fraction," *Remote Sens. Environ.*, vol. 80, no. 1, pp. 76–87, 2002.

[36] B. Martínez, F. Baret, F. Camacho-de Coca, F. J. García-Haro, A. Verger, and J. Meliá, "Validation of MSG vegetation products Part I. Field retrieval of LAI and FVC from hemispherical photographs," in *Proc. Remote Sens. for Agriculture, Ecosystem and Hydrol.*, Bellingham, WA, 2004, vol. 5568, pp. 57–68.

[37] F. Camacho-De Coca, F. J. García-Haro, M. A. Gilabert, and J. Meliá, "Vegetation cover seasonal changes assessment from TM imagery in a semi-arid landscape," *Int. J. Remote Sens.*, vol. 25, no. 17, pp. 3451–3476, Sep. 2004.

[38] D. E. Sabol, A. R. Gillespie, J. B. Adams, M. O. Smith, and C. J. Tucker, "Structural stage in Pacific Northwest forests estimated using simple mixing models of multispectral images," *Remote Sens. Environ.*, vol. 80, no. 1, pp. 1–16, Apr. 2002.

[39] A. Plaza, P. Martínez, R. Pérez, and J. Plaza, "Spatial/spectral endmember extraction by multidimensional morphological operations," *IEEE Trans. Geosci. Remote Sens.*, vol. 40, no. 9, pp. 2025–2041, Sep. 2002.

[40] A. Plaza, P. Martínez, R. Pérez, and J. Plaza, "A quantitative and comparative analysis of endmember extraction algorithms from hyperspectral data," *IEEE Trans. Geosci. Remote Sens.*, vol. 42, no. 3, pp. 650–663, Mar. 2004.

[41] S. J. Hook, *ASTER Spectral Library*. [Online]. Available: http://speclib.jpl.nasa.gov

[42] J. C. Jiménez-Muñoz, J. A. Sobrino, L. Guanter, J. Moreno, A. Plaza, and P. Martínez, "Fractional vegetation cover estimation from PROBA/CHRIS data: Methods, analysis of angular effects and application to the land surface emissivity retrieval," in *Proc. 3rd Workshop CHRIS/Proba*, Frascati, Italy, 2005. CD-ROM.

[43] J. A. Sobrino, J. C. Jiménez-Muñoz, J. Labed-Nachbrand, and F. Nerry, "Surface emissivity retrieval from digital airborne imaging spectrometer data," *J. Geophys. Res.*, vol. 107, no. D23. 4729, Dec. 2002. DOI:10.1029/2002JD002197.
[44] J. A. Sobrino, J.C. Jiménez-Muñoz, G. Sòria, M. Gómez, A. Barella-Ortiz, M. M. Zaragoza-Ivorra, Y. Julien, and J. Cuenca, "Thermal remote sensing in the framework of the SEN2FLEX Project: Field measurements, airborne data and applications," *Int. J. Remote Sens*., to be published.
[45] C. I. Gove, S. J. Hook, and E. D. Paylor, II, *The JPL Spectral Library*. [Online]. Available: http://speclib.jpl.nasa.gov/documents/jpl_desc.htm
[46] J. A. Sobrino, J. C. Jiménez-Muñoz, P. J. Zarco-Tejada, G. Sepulcre-Cantó, and E. de Miguel, "Land surface temperature derived from airborne hyperspectral scanner thermal infrared data," *Remote Sens. Environ.*, vol. 102, no. 1/2, pp. 99–115, May 2006.

José A. Sobrino is a Professor of physics and remote sensing and the Head of the Global Change Unit, University of Valencia, Valencia, Spain. He is the author of more than 100 papers. He is the Coordinator of the European projects WATERMED and EAGLE. He was the Chairperson of the First and Second International Symposium of the Recent Advances in Quantitative Remote Sensing. His research interest include atmospheric correction in visible and infrared domains, the retrieval of emissivity and surface temperature from satellite images, and the development of remote sensing methods for land cover dynamic monitoring.

Dr. Sobrino has been a member of the Earth Science Advisory Commitee (ESAC), European Space Agency (ESA) since November 2003.

Juan C. Jiménez-Muñoz received the Ph.D. degree in physics from the University of Valencia, Valencia, Spain, in 2005.

He is currently a Research Scientist with the Global Change Unit, Department of Earth Physics and Thermodynamics, University of Valencia. His main research interests include thermal remote sensing and temperature/emissivity retrieval.

Guillem Sòria received the Ph.D. degree in physics from University of Valencia, Valencia, Spain, in 2006.

He is currently a Research Scientist with the Global Change Unit, Department of Earth Physics and Thermodynamics, University of Valencia. His research interest includes the retrieval of surface temperature, including land, ice, and sea through multichannel and multiangle algorithms from thermal infrared remote sensed data supplied by ATSR-1, ATSR-2, and ENVISAT-AATSR sensors.

Mireia Romaguera received the degree in physics from the University of Valencia, Valencia, Spain, in 2002, the degree in physics from the University of Leeds, Leeds, England, in 2001, and the Ph.D. degree in physics from the University of Valencia, in 2006.

She is currently a Research Scientist in the Global Change Unit, Department of Earth Physics and Thermodynamics, University of Valencia. Her current research interest includes the retrieval of surface temperature, atmospheric water vapor content, and surface emissivity from an MSG1-SEVIRI sensor.

Luis Guanter received the B.Sc. degree (first-class honors) in physics and the M.Sc. and Ph.D. degrees in environmental physics and thermodynamics from the University of Valencia, Valencia, Spain, in 2002, 2004, and 2007, respectively.

He is currently with GeoForschungsZentrum-Potsdam, Germany. His research interests include atmospheric correction of satellite and airborne data, retrieval of atmospheric components, atmospheric radiative transfer modeling, and sensor calibration.

José Moreno (A'99) is currently a Professor of earth physics with the University of Valencia, Burjassot, Valencia, Spain. His main work is related to the modeling and monitoring of land surface processes. He has been involved in many international projects and research networks, being a Principal Investigator for ENVISAT and PROBA/CHRIS projects, as well as being responsible for the DAISEX and SPARC European Space Agency (ESA) campaigns. From 1995 to 1996, he was a Visiting Scientist with the NASA Jet Propulsion Laboratory. He is the author of many publications in the field, including several book chapters.

Dr. Moreno has been a member of the ESA Earth Sciences Advisory Committee from 1998 to 2002, the Space Station Users Panel, and other international advisory committees. He was an Associate Editor for the IEEE TRANSACTIONS ON GEOSCIENCE AND REMOTE SENSING from 1994 to 2000.

Antonio Plaza (M'05–SM'07) received the M.S. and Ph.D. degrees in computer science from the University of Extremadura, Cáceres, Spain, in 1997 and 2002, respectively.

He was a Visiting Researcher with the Remote Sensing Signal and Image Processing Laboratory, University of Maryland Baltimore County, Baltimore, the Applied Information Sciences Branch, Goddard Space Flight Center, Greenbelt, MD; and the AVIRIS Data Facility, Jet Propulsion Laboratory, Pasadena, CA. Since 2000, he has been an associate professor with the Department of Computer Science, University of Extremadura, where he was an assistant professor from 1997 to 1999. He is the author or coauthor of more than 140 publications including journal papers and conference proceedings. He is coediting (with Prof. C.-I Chang) a book on high performance computing in remote sensing (Chapman & Hall/CRC Press) and a special issue on high performance computing for hyperspectral imaging for the *International Journal of High Performance Computing Applications.* He is the Coordinator of Hyperspectral Imaging Network, a European project designed to build an interdisciplinary research community focused on hyperspectral imaging activities. His research interests include remote sensing, image processing, and efficient implementation of large-scale scientific problems on parallel and distributed systems.

Dr. Plaza is an Associate Editor for the IEEE TRANSACTIONS ON GEOSCIENCE AND REMOTE SENSING on hyperspectral image analysis and signal processing.

Pablo Martínez received the Ph.D. degree in physics from the University of Granada, Granada, Spain, in 1992.

He was a Visiting Researcher at the Applied Information Sciences Branch, Goddard Space Flight Center, Greenbelt, MD; the Department of Electrical Engineering, University of Maryland, College Park; and the AVIRIS Group, Jet Propulsion Laboratory, Pasadena, CA. He has been a Professor of computer science with the University of Extremadura, Cáceres, Spain, since 1985. He is currently the Head Scientist of the Neural Networks and Signal Processing Group (GRNPS). His main research interests include remote sensing, digital image analysis, hardware-based architectures, operating systems management and configuration, and neural-network-based pattern recognition.

Dr. Martínez has been a reviewer for the IEEE TRANSACTIONS ON GEOSCIENCE AND REMOTE SENSING.